



Highly nanotextured β -Bi₂O₃ pillars by electrostatic spray deposition as photoanodes for solar water splitting



Min-Woo Kim^{a,1}, Bhavana Joshi^{a,1}, Edmund Samuel^a, Karam Kim^a, Yong-Il Kim^a,
Tae-Gun Kim^a, Mark T. Swihart^b, Sam S. Yoon^{a,*}

^a School of Mechanical Engineering, Korea University, Seoul, 02841, Republic of Korea

^b Department of Chemical & Biological Engineering, University at Buffalo, The State University of New York, Buffalo, NY, 14260-4200, USA

ARTICLE INFO

Article history:

Received 8 March 2018

Received in revised form

4 June 2018

Accepted 5 June 2018

Available online 7 June 2018

Keywords:

Tetragonal Bi₂O₃

Pillar morphology

Electrostatic spray deposition

Water splitting

Photocurrent

Mott-Schottky analysis

ABSTRACT

We demonstrate fabrication of films of highly textured bismuth oxide (Bi₂O₃) pillars via electrostatic spray deposition and test the performance of these films as photoanodes in photoelectrochemical water splitting. The β -Bi₂O₃ and α -Bi₂O₃ phases were identified and distinguished using X-ray diffraction, Raman spectroscopy, and transmission electron microscopy. The β -Bi₂O₃ pillars of optimized thickness exhibited a photocurrent density of 0.97 mA·cm⁻² at 0.5 V vs Ag/AgCl. The tetragonal β -Bi₂O₃ pillars had enhanced visible light absorbance compared to α -Bi₂O₃ as well as other metal oxides like ZnO and TiO₂. Tauc plot analysis of film absorbance showed a decrease in the bandgap of the β -Bi₂O₃ phase to 2.5 eV. In Na₂SO₃ electrolyte, a hole scavenger, the onset voltage for the β -Bi₂O₃ phase was shifted to a more negative value (−0.4 V), which increased photocurrent density. The electron concentration reached its highest value of 9.1×10^{20} cm⁻³ for the film with the highest photocurrent density.

© 2018 Elsevier B.V. All rights reserved.

1. Introduction

The use of semiconductors in photoelectrochemical (PEC) devices coupled with photovoltaics provides a means of producing hydrogen from water using only solar energy. The most common semiconducting materials for solar water splitting include ZnO, TiO₂, BiVO₄, CuO, and Fe₂O₃ [1,2]. Widely used metal oxides such as ZnO and TiO₂ have bandgaps of ~3 eV, and therefore capture only ultraviolet (UV) light, which makes up a small portion of the solar spectrum. However, bismuth oxide (Bi₂O₃) polymorphs (α -, β -, γ -, δ -, ω -, and ϵ -Bi₂O₃) have lower bandgaps, and can capture both UV and visible light. Among them, β -Bi₂O₃ has a bandgap near 2.5 eV, and can therefore absorb a greater portion of the solar spectrum than oxides like ZnO and TiO₂ [3,4]. In addition, Bi₂O₃ is nontoxic and has high refractive index, dielectric permittivity, and ionic and photonic conductivity, suggesting promise as a candidate anode material for photo-induced water splitting [5,6]. However, its high-refractive index may also lead to high reflection and optical losses [7]. Nanostructuring can reduce optical losses by enhancing the

optical mode density over a broad range of wavelengths. Furthermore, pillars comprised of nanoparticles can improve the light absorbance significantly [7,8].

In all polymorphs of Bi₂O₃, the valence band is composed of O 2p and Bi 6s orbitals, while the conduction band is comprised of Bi 6p levels. Compared to other polymorphs, the valence band of β -Bi₂O₃ is shifted to higher energy, yielding a smaller bandgap value. This phase also exhibits enhanced electron transport arising from its *c*-axis oriented tetragonal structure [9,10]. The electron mobility under irradiation is also enhanced by the lone-pair electrons (Bi 6s) present in the valence band [11]. The high photoconductivity of β -Bi₂O₃ is attributed to its intrinsic polarizability and tetragonal structure, both of which favor the separation of photogenerated electron–hole pairs. Moreover, the lone pair in Bi provides a channel for photo-excited electron transport and reduces electron–hole recombination. Along with the many advantages of β -Bi₂O₃ as a semiconducting PEC material, the β -Bi₂O₃ phase has one key disadvantage. The β -Bi₂O₃ is metastable at ambient conditions and thus may not be maintained over long periods of use [1,9,12,13].

Light absorbance is highly dependent on the morphology of Bi₂O₃ films. Bi₂O₃ nanostructures including nanotubes [14,15], nanoparticles [16,17], nanowires [18], and nanorods [19,20] have

* Corresponding author.

E-mail address: skyoons@korea.ac.kr (S.S. Yoon).

¹ These authors have contributed equally.

been produced by techniques including hydrothermal methods [1], microwave-assisted assembly [21], atomic layer deposition [22], microemulsion [23], and sol-gel processing [24]. However, most of these processes require multiple complex steps, harsh reaction conditions, and long synthesis times to achieve the desired morphologies and photocatalytic activities. A simple yet effective nanostructure fabrication route is necessary for the practical use of Bi_2O_3 for PEC applications.

Here, we demonstrate for the first time the fabrication of pillar-shaped Bi_2O_3 nanostructures using a simple and scalable non-vacuum electrostatic spray deposition (ESD) technique. The features and advantages of ESD have been described in our previous studies [8,25–28] which showed that ESD can consistently produce pillar-shaped BiVO_4 and Bi_2WO_6 by combined diffusive, thermophoretic, and electrophoretic transport of electro sprayed precursor droplets [25,28,29]. Post-annealing treatment of electro sprayed Bi_2O_3 induces phase transformation into the α - or β - Bi_2O_3 phase, depending on the annealing temperature. We focus on producing the β - Bi_2O_3 phase, which is known to permit the highest photocurrent density (PCD) among Bi_2O_3 polymorphs. Then, the thickness of films comprised of these nanopillars was tuned by varying the electro spraying time between 15 and 120 min to identify the optimal thickness. Results are also compared to PCD values from prior studies [30–34].

2. Experimental section

2.1. Deposition of Bi_2O_3 films

The precursor solution for the Bi_2O_3 films was prepared by mixing 1.08 g of bismuth(III) nitrate pentahydrate ($\text{Bi}(\text{NO}_3)_3 \cdot 5\text{H}_2\text{O}$, $\geq 98\%$, Sigma-Aldrich) in 10 mL acetic acid (CH_3COOH , 99.7%, Samchun Chemicals) at 25 °C (room temperature, RT) with stirring at 500 rpm for 30 min. The complete dissolution of $\text{Bi}(\text{NO}_3)_3$ in CH_3COOH produced a transparent solution. The precursor solution was then deposited on a pre-cleaned indium tin oxide (ITO) glass substrate measuring $2.5 \times 2.5 \text{ cm}^2$, by the ESD process. The solution was delivered at a flowrate of 45 $\mu\text{L}/\text{h}$ through a 4 mm diameter nozzle. The nozzle-to-substrate distance was 4.5 cm and the substrate temperature was maintained at 50 °C. A stable Taylor cone was achieved upon application of a high voltage of 11.1 kV. ESD coating times of 15, 30, 60, 90, and 120 min were tested. Fig. 1a schematically illustrates precursor preparation, ESD, and annealing.

The as-deposited (as-dep) Bi_2O_3 was white in color. To investigate the effect of annealing, samples were annealed at 370, 400, 430, and 460 °C for 1 h. Fig. 1b shows samples before and after annealing. The Bi_2O_3 film annealed at 430 °C became yellow in color and scanning electron microscopy (SEM) imaging showed the pillar-like morphology of the film.

2.2. Characterization of Bi_2O_3 films

The crystalline structures of the films were analyzed by X-ray diffraction (XRD, Rigaku, Japan, D/max-2500) with $\text{Cu K}\alpha$ radiation over a diffraction angle (2θ) range of 20°–65°. The absorbance of films was measured by UV–vis spectroscopy (Optizen POP Mecasys Co. LTD, Korea). X-ray photoelectron spectroscopy (XPS, X-TOOL, ULVAC-PHI) was employed to determine the surface chemical states of the films. Raman spectra of the films were acquired using a LabRam ARAMIS IR2 spectrometer (Horiba Jobin Yvon) with a 532 nm laser source. The Bi_2O_3 films were characterized by transmission electron microscopy (TEM, JEM 2100F, JEOL Inc.) to obtain high-resolution TEM (HRTEM) images and selected-area electron diffraction (SAED) patterns. The morphologies of the Bi_2O_3 films were also analyzed using high-resolution SEM (HR-SEM, XL30 SFEQ, Phillips Co., Holland) at 15 kV. PEC performance of Bi_2O_3 films was assessed by measuring PCD during water splitting. The annealed Bi_2O_3 films were used as working electrodes, with a Ag/AgCl reference electrode and Pt wire counter electrode. The PEC measurements were performed in 0.5 M Na_2SO_4 (pH = 7) or 1 M Na_2SO_3 (pH = 9) as the electrolyte. A Xe arc lamp (Newport, Oriel Instruments, USA) equipped with an AM 1.5 filter was used to mimic sunlight with a light intensity of 100 mW/cm^2 . The PCD was measured using a potentiostat (VersaSTAT-3, Princeton Applied Research, USA) for applied voltages of –0.4 to 1.2 V (vs. Ag/AgCl) at a scan rate of 10 mV/s . Mott–Schottky and electrochemical impedance spectroscopy (EIS) measurements were performed using the aforementioned potentiostat and the same electrode configuration.

3. Results and discussion

3.1. Film characterization

The crystallographic phases of the as-deposited and annealed Bi_2O_3 films were characterized by X-ray diffraction (XRD). Fig. 2a

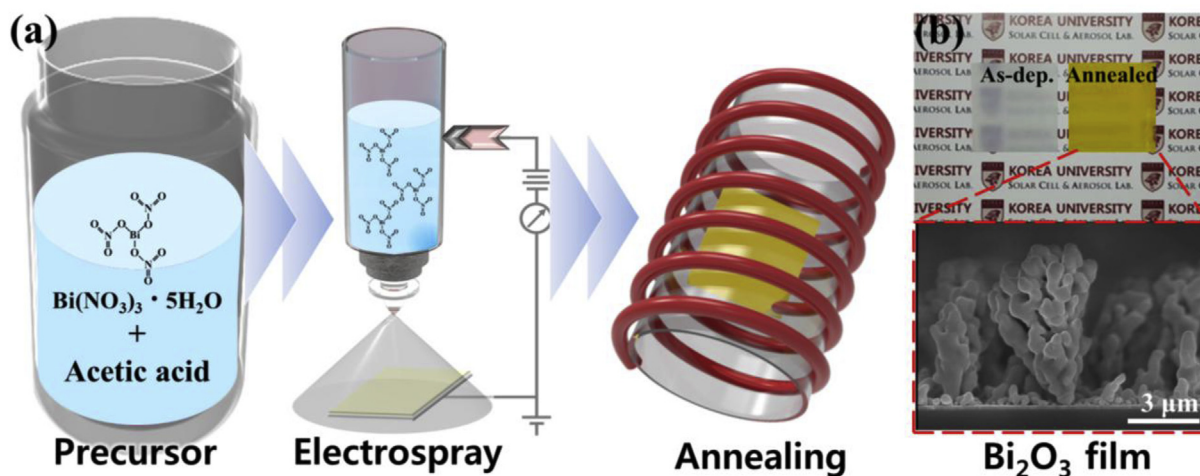


Fig. 1. (a) Schematics showing the ESD setup for Bi_2O_3 deposition and annealing, (b) photograph of as-deposited and annealed films and (inset) cross-sectional micrograph of film morphology.

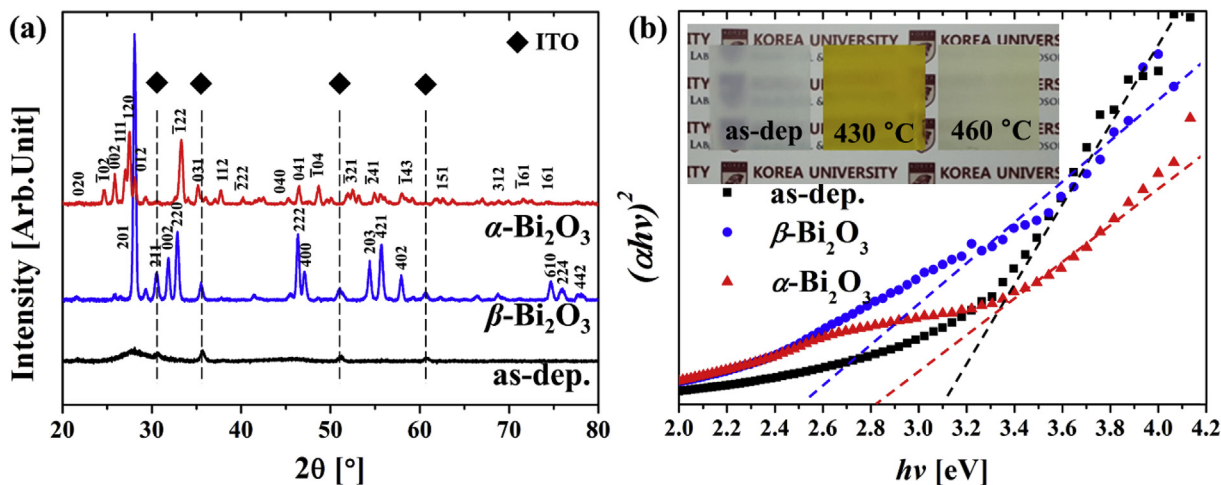


Fig. 2. (a) XRD patterns and (b) Tauc plots of $(\alpha h\nu)^2$ vs. $h\nu$ for as-deposited film and α - and β - Bi_2O_3 films produced by annealing at 430 and 460 °C, respectively.

shows two XRD patterns with well-defined peaks, from the films annealed at 430 °C (blue) and 460 °C (red), which correspond to the β and α - Bi_2O_3 phases, respectively. The black XRD pattern from the as-deposited film shows that it is amorphous. The substrate temperature of 50 °C is insufficient for Bi_2O_3 crystallization; hence, only peaks associated with the ITO substrate are visible. This amorphous phase remained unchanged with annealing at 370 and 400 °C, as

shown in Fig. S1. The peaks observed for the film annealed at 430 °C can be indexed to the tetragonal crystal structure of metastable β - Bi_2O_3 (JCPDS No. 27-0050). At the annealing temperature of 460 °C, restructuring occurs and β - Bi_2O_3 is transformed to the stable monoclinic α - Bi_2O_3 phase, as observed by peaks matching JCPDS No. 41-1449. The results are consistent with references [1,35] that report similar metastable-to-stable Bi_2O_3 phase transitions over

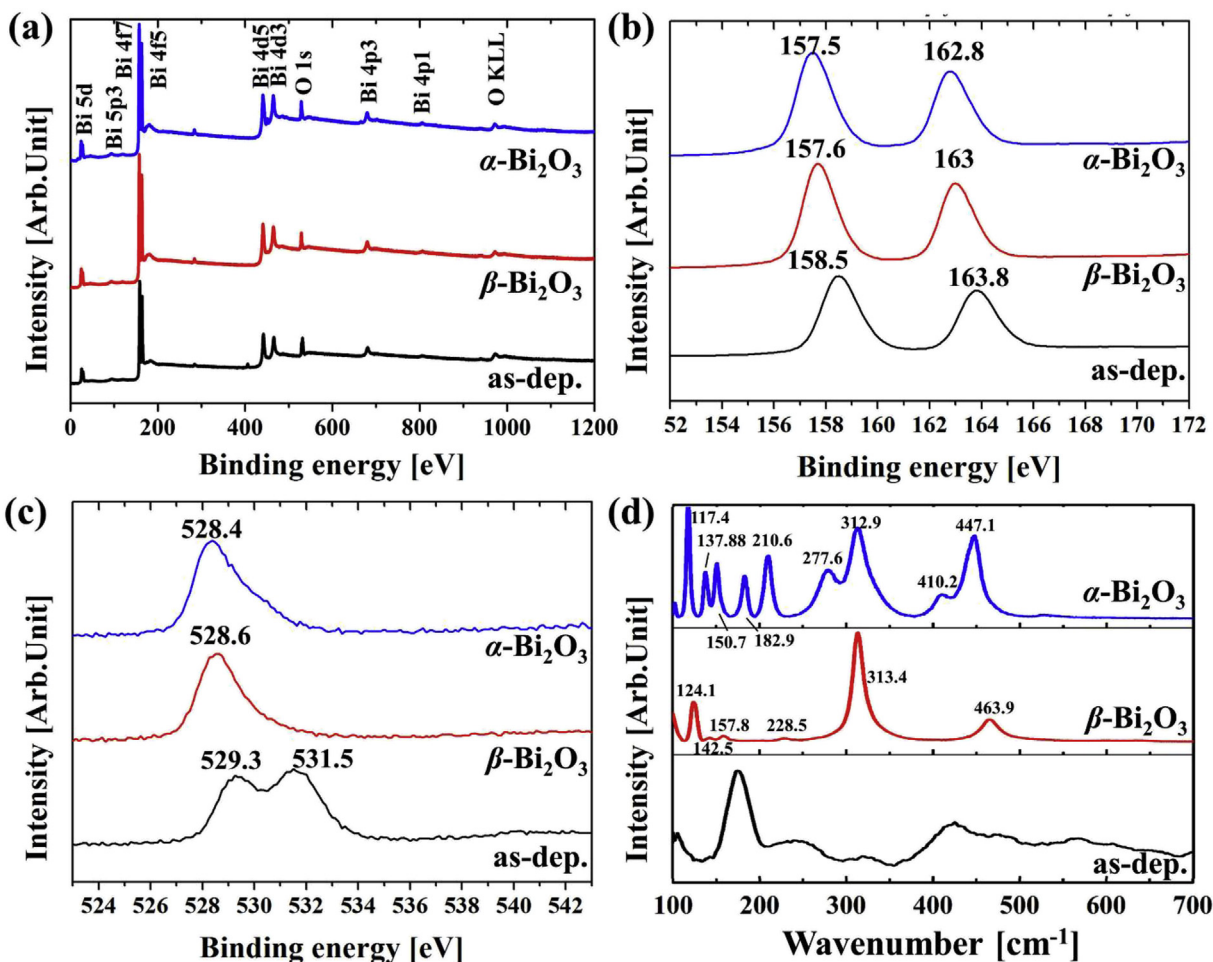


Fig. 3. XPS spectra: (a) survey and core-level spectra of: (b) Bi 4f and (c) O 1s. (d) Raman spectra of amorphous, β - Bi_2O_3 , and α - Bi_2O_3 films.

similar temperature ranges, with some variation depending on the synthesis method.

The bandgap energies of different phases of Bi_2O_3 were determined from the Tauc plot ($(\alpha hv)^2$ vs. hv) shown in Fig. 2b, based on the absorption spectra in the UV–visible region (see Fig. S2). In this analysis, the band gap is estimated as the x -intercept of the line tangent to the $(\alpha hv)^2$ vs. hv curve. The films annealed at 430 °C and 460 °C, corresponding to the β and α phases of Bi_2O_3 , show bandgaps of 2.5 and 2.8 eV, respectively. The as-deposited amorphous Bi_2O_3 shows the highest bandgap of 3.1 eV. The bandgaps for the different phases obtained here are consistent with previous reports [4,12]. The narrower bandgap of β - Bi_2O_3 permits absorbance of more visible light to generate charge carriers. The as-deposited film without heat treatment is white in color, but is transformed to yellow and beige with annealing at 430 °C and 460 °C, respectively, as depicted in the inset of Fig. 2b. This change is due to the transformation in the crystal structure of Bi_2O_3 and is consistent with previous reports [31].

XPS was performed to identify the chemical states of the Bi_2O_3 polymorph films. Fig. 3a shows the survey spectra of the samples; the presence of Bi and O peaks confirms the formation of Bi_2O_3 in all films. The Bi 4f core-level XPS spectrum in Fig. 3b shows two characteristic narrow Gaussian-shaped near-symmetrical peaks at 157.7 and 163 eV, corresponding to Bi 4f_{7/2} and Bi 4f_{5/2} in the β - Bi_2O_3 film, which match prior reports [36–38]. Further, no peaks of bi-, tetra-, or pentavalent Bi states are observed on the Bi 4f_{7/2} shoulder, and the binding energy difference of 5.3 eV confirms that Bi exists in the Bi^{3+} oxidation state in all samples [38]. However, the

as-deposited film shows higher binding energies of 158.5 and 163.8 eV, indicating higher electronegativity, as Bi is connected to more O atoms and impurities [6]. Fig. 3c shows the O 1s core spectra, which indicate that increasing the annealing temperature decreases the O content [39]. In the as-deposited film, well-resolved peaks at 529.5 and 531.5 eV are observed from functional impurities and O–H components, arising from non-volatile reactants remaining after deposition [40]. However, after annealing, the Bi–O lattice O is evident from the peaks at 528.4 and 528.6 eV for α - and β - Bi_2O_3 , respectively [41].

The Raman spectra of the amorphous, β -, and α - Bi_2O_3 films were recorded under 532 nm excitation over the wavenumber range of 100–700 cm^{-1} , as shown in Fig. 3d. The as-deposited film exhibits broad Raman bands at 175, 250, and 410 cm^{-1} , possibly from non-volatile impurities and the broad distribution of Bi–O bond lengths. For β - and α - Bi_2O_3 , distinct Raman modes are observed. The spectrum of β - Bi_2O_3 shows prominent Raman bands at 124, 142, 157, 228, 313, and 464 cm^{-1} , corresponding to the displacement of O atoms bonded with Bi, i.e. the stretching of Bi–O bonds [42,43]. The spectrum of α - Bi_2O_3 shows Raman features at 117, 137, 150, 210, 227, 312, 410, and 467 cm^{-1} . The 117 cm^{-1} mode arises from A_g symmetric motion of Bi atoms. Modes of 137 (A_g) and 150 cm^{-1} (B_g) arise from displacements of both Bi and O atoms in α - Bi_2O_3 . The Raman peaks at higher frequencies (210, 312, 410, and 467 cm^{-1}) are attributed to the displacement of the O atoms in α - Bi_2O_3 . Thus, similar to the XRD patterns, the Raman features also confirm the formation of β - and α - Bi_2O_3 at annealing temperatures of 430 and 460 °C, respectively [44,45].

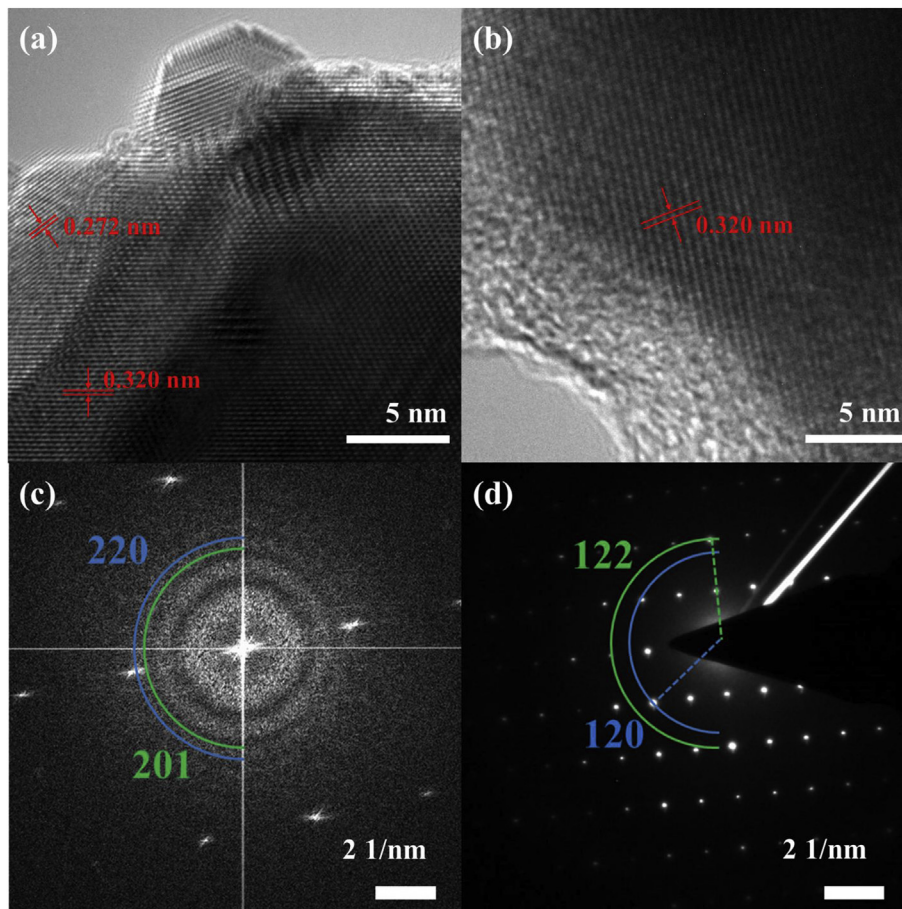


Fig. 4. (a, b) HRTEM images and (c, d) SAED patterns of (a, c) β - Bi_2O_3 and (b, d) α - Bi_2O_3 .

Local structural information for β - Bi_2O_3 and α - Bi_2O_3 was provided by HRTEM imaging and SAED pattern analysis. The HRTEM images in Fig. 4a and Fig. 4b clearly depict lattice fringes showing the crystallinity of Bi_2O_3 . The lattice spacings of 0.272 and 0.323 nm correspond to the (201) and (220) planes, respectively, of β - Bi_2O_3 (Fig. 4a). The lattice spacing of 0.319 nm, observed in Fig. 4b, is attributed to the (120) planes of α - Bi_2O_3 . Fig. 4c shows diffuse diffraction rings in the SAED pattern of β - Bi_2O_3 , corresponding to the (201) and (220) planes and demonstrating the polycrystalline nature of the film. The SAED pattern in Fig. 4d of α - Bi_2O_3 shows a distinct dot pattern indexed to the (120) and (122) crystal planes of α - Bi_2O_3 .

Fig. 5a–e presents cross-sectional images of the β - Bi_2O_3 films deposited for 15, 30, 60, 90, and 120 min. The images show that, with increasing coating time, the thickness of the film as well as the grain size increases. Initially, the deposited particles form a layer of ~ 200 nm; then, subsequent particles are adhered to the first accumulated particles to form pillar shapes. Distinct pillar formation occurs after 30 min of film coating. Formation of this morphology results from simultaneous diffusive, thermophoretic, and electrophoretic transport of evaporating charged droplets as discussed in our prior studies [25]. These pillars are expected to increase the number of available reaction sites because they are separated by lateral uncoated spaces, which can provide greater access to the electrolyte and thus increase O_2 evolution during PCD testing. Top surface view SEM images of the β - Bi_2O_3 films obtained at different coating times are presented in the insets of Fig. 5, and illustrate the 2D to 3D transformation of the surface due to pillar growth. The effect of deposition time on film thickness is presented in Fig. 5f. The thickness is increased from 0.2 μm for a 15 min deposition to 6.5 μm for a 120 min deposition. The superlinear increase in film thickness with deposition time arises from the open, pillared morphology of the film, in which average film density decreases with increasing thickness and deposition time.

3.2. PEC properties

To achieve clean energy from PEC systems, the photoanode must demonstrate fast charge transfer and efficient electron–hole pair separation with a slow electron–hole recombination rate at the surface. The photoanode demonstrated here has a distinctive pillar morphology that enhances photocatalytic performance by providing short hole-transport pathways to the surface for O_2 evolution. The monoclinic α - Bi_2O_3 and tetragonal β - Bi_2O_3 films obtained after annealing were tested by measuring PCD during water splitting in a 0.5-M Na_2SO_4 electrolyte, as presented in Fig. 6a. Although both samples had the same spraying time of 90 min, α - Bi_2O_3 shows a PCD of $0.025 \text{ mA}\cdot\text{cm}^{-2}$ at 1.2 V (vs. Ag/AgCl), which is a modest increase from the dark current, while β - Bi_2O_3 shows a PCD of $0.1 \text{ mA}\cdot\text{cm}^{-2}$, approximately four times greater than that of α - Bi_2O_3 . We attribute the lower PCD of α - Bi_2O_3 to its lower absorption coefficient and higher bandgap compared to those for β - Bi_2O_3 , as shown in Fig. 2b. The performance of the photoanode fabricated with tetragonal β - Bi_2O_3 is superior to that of monoclinic α - Bi_2O_3 . The dark current is negligible in both cases. The increased visible-light harvesting by β - Bi_2O_3 is attributed to its lower bandgap and tetragonal structure, which facilitates fast hole transport. The potentials shown are with reference to the Ag/AgCl electrode. They can be converted to potentials relative to a reversible hydrogen electrode (RHE) through the following expression: $E_{\text{RHE}} = E_{\text{Ag/AgCl}} + 0.059 \text{ pH} + 0.1976$, where E_{RHE} is the potential vs the RHE, $E_{\text{Ag/AgCl}}$ is the potential vs. the Ag/AgCl electrode, and pH is the numeric scale potential of hydrogen for the Na_2SO_4 electrolyte solution. The peak at 0.33 V appearing during the PEC testing of tetragonal β - Bi_2O_3 could be due to oxidative dissolution of Bi to Bi^{3+} in presence of 0.5 M Na_2SO_4 electrolyte where Bi^{3+} can react with 2 h^+ to form Bi^{5+} [46,47]. However, in the presence of Na_2SO_3 , electrolyte holes are scavenged and formation of Bi^{5+} is avoided [47].

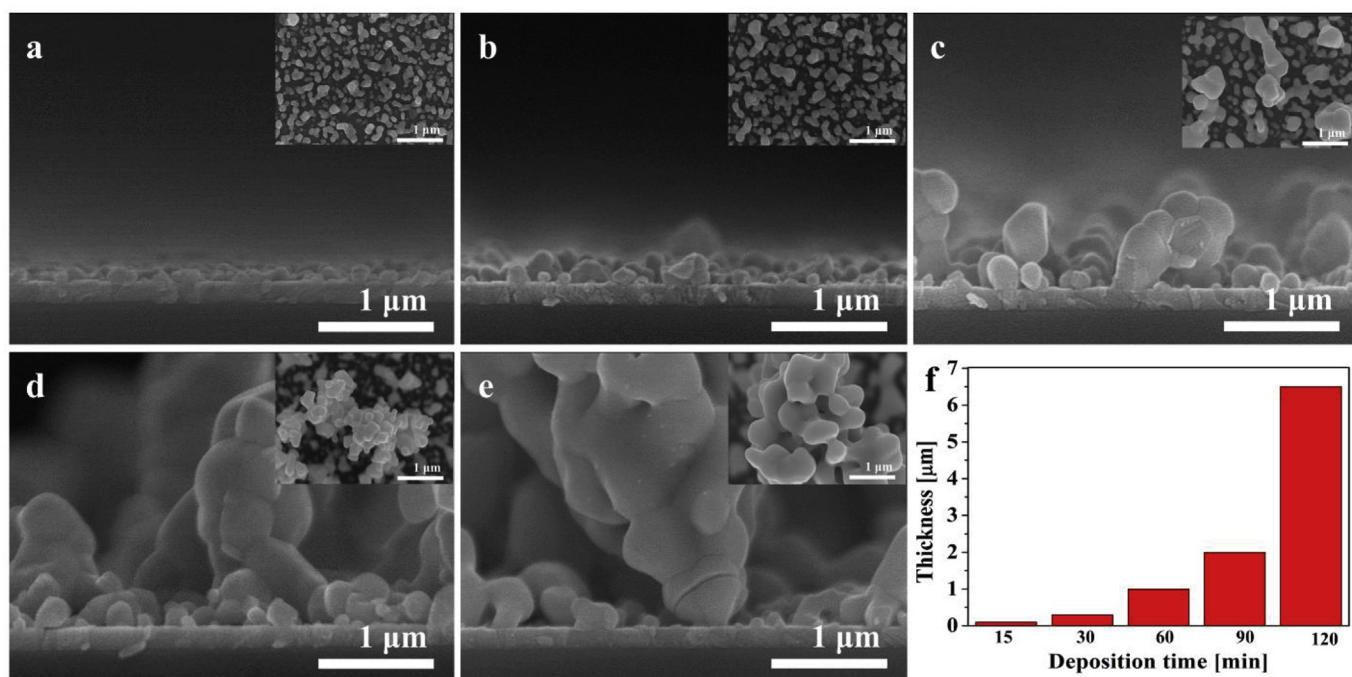


Fig. 5. SEM cross-sectional views of β - Bi_2O_3 films deposited for (a) 15, (b) 30, (c) 60, (d) 90, (e) and 120 min; insets show surface views of each film. (f) Comparison of film thicknesses for each deposition time.

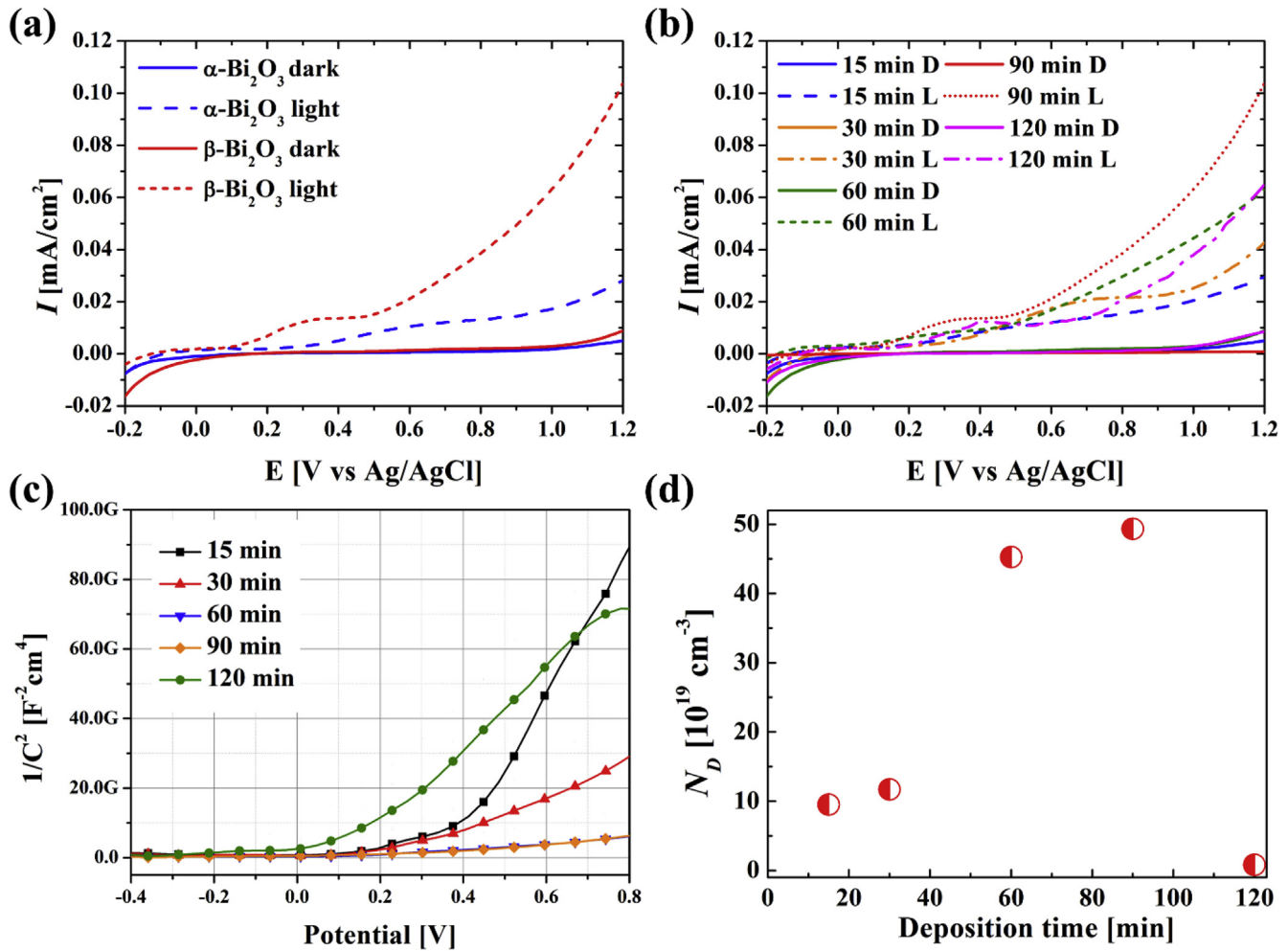


Fig. 6. Plots of PCD vs. applied potential (vs. Ag/AgCl) (a) for different phases of Bi_2O_3 deposited for 90 min, (b) for β - Bi_2O_3 deposited for different times, (c) Mott–Schottky graph, and (d) electron concentration (N_D) determined from slopes of Mott–Schottky plots for films obtained after different deposition times.

The thickness optimization of β - Bi_2O_3 to achieve the optimum PCD is presented in Fig. 6b. The dark currents for the samples of various thicknesses were almost identical. Fig. 6b reveals that, with increasing film deposition time from 15 to 90 min, the PCD increases to a maximum of 0.1 mA·cm⁻². However, the sample with 120 min deposition time shows a decreased PCD, possibly from the increased pillar height, which decreases the electric field and subsequently induces faster charge recombination before holes can reach the pillar surface. The better performance of the sample produced by 90 min of deposition can also be attributed to enhanced lifetime as deduced from photoluminescence (PL) measurements. PL measurements showing the emission intensities or transition probabilities are presented in Fig. S3. The PL lifetime increased with increasing deposition time as shown in Fig. S3. However, for deposition time of 120 min the lifetime began to decline, perhaps due to the bulk-like characteristics of the very thick film (see Fig. 5f), which could reduce surface-trapping of separated charge carriers and promote recombination at bulk defects [48,49]. The film samples deposited for 15 and 30 min were thin, as shown in the SEM images (see Fig. 5), which could permit fast electron tunneling at the electrode/electrolyte surface, thus hampering electron–hole separation. Of course, thinner films also absorb less light. The gradual increase in thickness was accompanied by a decrease in capacitance at the Helmholtz layer, as

observed from the Mott–Schottky (MS) plot in Fig. 6c, suggesting an increased electron concentration for β - Bi_2O_3 .

Mott–Schottky plots show the dependence of the space charge capacitance (C_{sc}) generated by the Helmholtz layer at the electrode/electrolyte interface on various semiconductor parameters, including the conduction-band potential $E(V)$ and the flat-band potential $E_{fb}(V)$, as expressed in the following equation:

$$\frac{1}{C_{sc}^2} = \left(\frac{2}{e\epsilon\epsilon_0 N_D} \right) \left(\frac{E - E_{fb} - kT}{e} \right) \quad (1)$$

where k is the Boltzmann constant, $T(K)$ is the absolute temperature, e is the charge of an electron (C), ϵ is the relative permittivity, ϵ_0 is the permittivity of vacuum, and N_D is the donor concentration per unit volume (cm⁻³). The x -axis intercept of the tangent of the Mott–Schottky curve indicates the E_{fb} of the sample. The slope of the Mott–Schottky curve allows determination of N_D for the material. N_D values for the β - Bi_2O_3 samples shown in Fig. 6d display significant variance, attributed to the increasing thickness of the films (see Fig. 5) in accordance with deposition time. However, regardless of the film thickness, the photoanodes show gradual increases in slope with increasing applied potential. This increase in slope suggests that N_D increases with increased biasing through ionization of donor levels. These Mott–Schottky plots support the

enhancement of PCD. The sample with the 120 min deposition time shows a decrease in both PCD and N_D . The decreased donor concentration of this sample may arise from the high crystallinity of the sample [50]. We also determined the carrier concentration through Hall-measurements, as shown in Fig. S4. The carrier concentrations obtained by Hall measurement are lower compared to those obtained from Mott–Schottky analysis. The higher carrier concentrations from Mott–Schottky analysis could be due to the presence of electrolyte under applied bias condition and the nonplanar surface of the nanostructured photoanodes. Interactions at the photoanode–electrolyte junction can result in the accumulation of the charges the interface [51].

PEC measurements for the β - Bi_2O_3 films were also performed in the presence of a sacrificial reagent, Na_2SO_3 , which acts as a hole scavenger through preferential oxidation of sulfite rather than water [52]. Fig. 7a shows the photocurrent–potential curve using 1-M Na_2SO_3 to reduce the impact of hole adsorption and the slow transfer kinetics under illumination at the interface region, which should increase the PCD of β - Bi_2O_3 [53]. In sulfite oxidation, the photocurrent initiation potential shifts to a negative value of approximately -0.4 V , compared to -0 V in Na_2SO_4 . Thus, the presence of Na_2SO_3 enhances the PEC performance by lowering the onset potential, which induces rapid electron transfer from the valence band to the conduction band under visible light. At 0.5 V vs.

Ag/AgCl , the PCD of β - Bi_2O_3 is $0.97\text{ mA}\cdot\text{cm}^{-2}$ in the Na_2SO_3 electrolyte. Fig. 7b shows results of a stability test in Na_2SO_3 electrolyte at an applied voltage of 0.3 V vs Ag/AgCl . Initially, the electrode shows a PCD of $0.5\text{ mA}\cdot\text{cm}^{-2}$, which decreases over time. Over 12000 s of voltage application, the PCD shows little evidence of photocorrosion. Fig. 7c shows the impedance response for frequencies from 100 kHz to 0.1 Hz . As reflected in the figure, the impedance of the β - Bi_2O_3 film in Na_2SO_4 is greater than that in Na_2SO_3 . The lower impedance response of the sample in Na_2SO_3 indicates the lower recombination rate promoted by the hole-scavenging characteristics of Na_2SO_3 , relative to that in Na_2SO_4 . This result further corroborates the improvement in PCD for β - Bi_2O_3 with the Na_2SO_3 electrolyte, as shown in Fig. 7a. The Nyquist plot data were fitted using a Randle equivalent circuit model (see inset of Fig. 7c). The resistance of the photoelectrode is denoted R_{sp} , while the charge transfer resistance (R_{ct}) is associated with Faradaic processes. The β - Bi_2O_3 photoelectrode solution resistance and charge transfer resistance with respect to different electrolytes are presented in the table shown as an inset of Fig. 7c.

Mott–Schottky analyses were performed without illumination in $0.5\text{-M Na}_2\text{SO}_4$ and $1\text{-M Na}_2\text{SO}_3$, as shown in Fig. 7d. In the presence of Na_2SO_3 , the flat-band potential shifts to a more negative value (-0.26 V) compared to that in Na_2SO_4 (-0.01 V). Therefore, the electron concentration increases with applied potential at

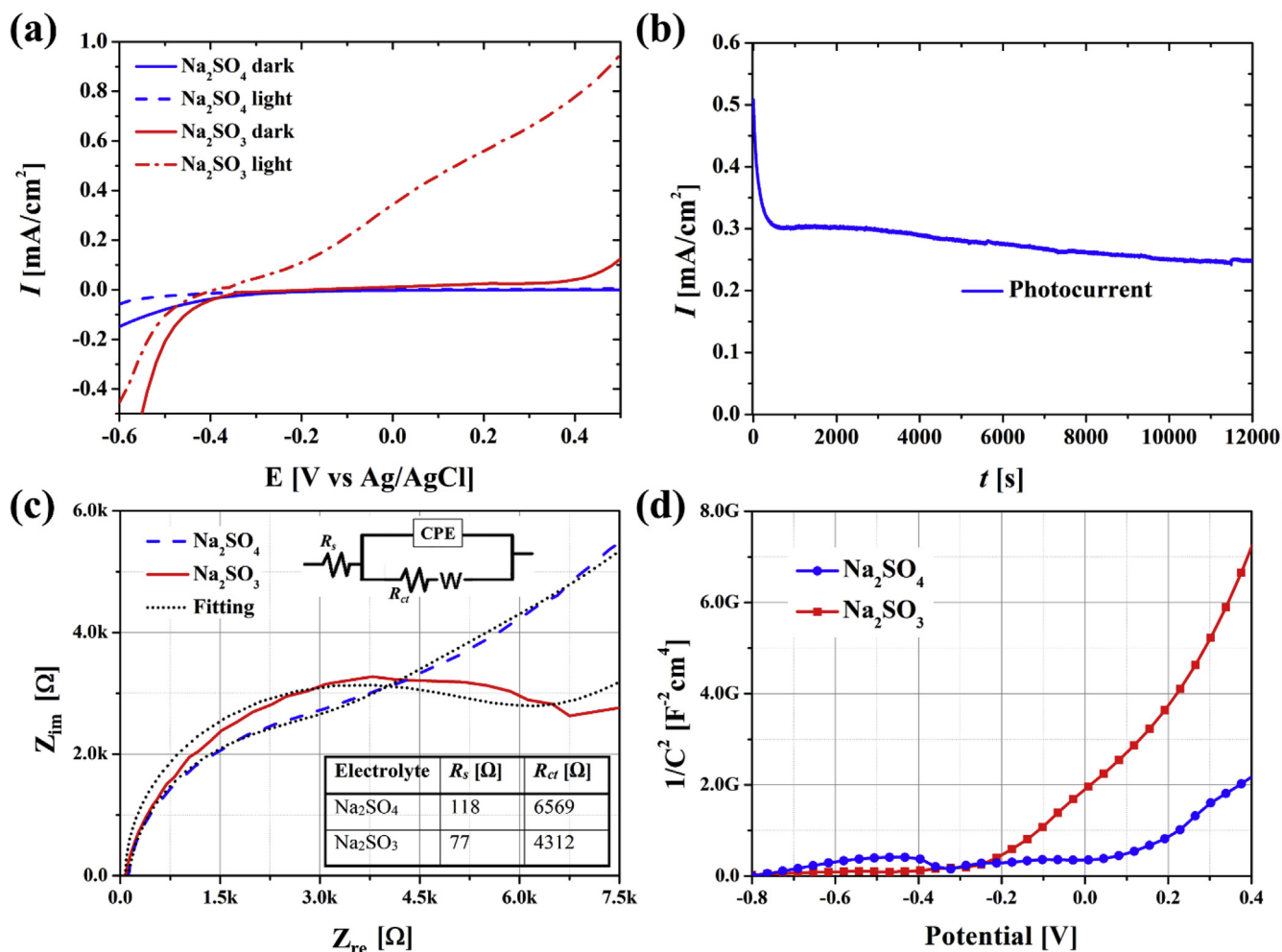


Fig. 7. (a) PEC response under dark and light conditions, (b) long term stability curve in Na_2SO_3 electrolyte at a potential of 0.3 V , (c) Nyquist plots, and (d) Mott–Schottky curves of β - Bi_2O_3 photoanodes. Na_2SO_4 and Na_2SO_3 are the two electrolytes used for respective measurements.

Table 1
Comparison of PCDs of various reported Bi₂O₃ films with present ESD-coated pillared film.

Materials	Electrolyte	PCD (mA·cm ⁻²)	Reference
Bi ₂ O ₃	0.5 M KOH	0.025 @ 0.5 V ^a	[30]
Bi ₂ O ₃ (UV illumination)	0.2 M Na ₂ SO ₃	0.00125 @ 0.6 ^b	[31]
Bi ₂ O ₃ /Bi (UV illumination)	0.5 M (NH ₄) ₂ SO ₄	0.021 @ 1.0 V ^b	[32]
Bi ₂ O ₃	0.5 M Na ₂ SO ₃	0.67 @ 1.23 V ^c	[33]
Bi ₂ O ₃	1 M KOH	0.97 @ 1.53 V ^d	[34]
Bi₂O₃	1 M Na₂SO₃	0.97 @ 0.5 V^a 0.97 @ 1.23 V^d	Present

^a vs. Ag/AgCl.

^b vs. SCE.

^c vs. NHE.

^d vs. RHE.

much lower potential in Na₂SO₃. The electron concentrations for the photoanode produced at a deposition time of 90 min are 49.3×10^{19} and 90.9×10^{19} cm⁻³ in Na₂SO₄ and Na₂SO₃, respectively. The enhancement of PCD with the hole-scavenging electrolyte can be attributed to lower hole absorption at the interface, higher electron concentration, and lower flat-band potential.

The PCD values of the Bi₂O₃ films produced by ESD in this study are compared with those of previously reported films in Table 1. Few reports are available on the PCD performance of Bi₂O₃, despite Bi₂O₃ being a well-studied photocatalyst in dye degradation [36,54–57]. The films synthesized in this study exhibit significantly better PEC performance than previously reported films.

4. Conclusions

We report for the first time the fabrication of pillar-structured Bi₂O₃ by a non-vacuum ESD technique. Films of the pillar-structured Bi₂O₃ show improved PCD of 0.97 mA·cm⁻² and enhanced visible light harvesting. The photoanode showed only slight PCD decay, with excellent stability over 12000 s. In this study, we confirmed that Bi₂O₃ films can be fabricated in different phases by controlling the annealing temperature after ESD. The PEC performance of β-Bi₂O₃ is superior to that of α-Bi₂O₃. Additionally, the tetragonal β-Bi₂O₃ demonstrates fast charge-transfer capability in EIS measurements performed in Na₂SO₃. The pillared morphology of β-Bi₂O₃ delivers a shorter charge-transfer pathway and a lower bandgap (2.5 eV). Thus, this optimized photoanode exhibiting high PCD and good stability shows promise for use in water splitting and clean energy applications.

Acknowledgment

This research was supported by the Technology Development Program to Solve Climate Changes of the National Research Foundation (NRF) funded by the Ministry of Science, ICT and Future Planning (NRF-2016M1A2A2936760) and NRF-2017R1A2B4005639.

Appendix A. Supplementary data

Supplementary data related to this article can be found at <https://doi.org/10.1016/j.jallcom.2018.06.047>.

References

[1] Y. Qiu, M. Yang, H. Fan, Y. Zuo, Y. Shao, Y. Xu, X. Yang, S. Yang, Nanowires of α- and β-Bi₂O₃: phase-selective synthesis and application in photocatalysis, *CrystEngComm* 13 (2011) 1843–1850.
[2] C. Jiang, S.J. Moniz, A. Wang, T. Zhang, J. Tang, Photoelectrochemical devices

for solar water splitting—materials and challenges, *Chem. Soc. Rev.* 46 (2017) 4645–4660.
[3] J. Zhang, W. Dang, X. Yan, M. Li, H. Gao, Z. Ao, Doping indium in β-Bi₂O₃ to tune the electronic structure and improve the photocatalytic activities: first-principles calculations and experimental investigation, *Phys. Chem. Chem. Phys.* 16 (2014) 23476–23482.
[4] J. Hou, C. Yang, Z. Wang, W. Zhou, S. Jiao, H. Zhu, In situ synthesis of α-β phase heterojunction on Bi₂O₃ nanowires with exceptional visible-light photocatalytic performance, *Appl. Catal., B* 142 (2013) 504–511.
[5] K.S. Al-Namshah, R.M. Mohamed, Nd-doped Bi₂O₃ nanocomposites: simple synthesis and improved photocatalytic activity for hydrogen production under visible light, *Appl. Nanosci.* (2018) 1–7.
[6] Y. Bao, T.-T. Lim, Z. Zhong, R. Wang, X. Hu, Acetic acid-assisted fabrication of hierarchical flower-like Bi₂O₃ for photocatalytic degradation of sulfamethoxazole and rhodamine B under solar irradiation, *J. Colloid Interface Sci.* 505 (2017) 488–499.
[7] M.L. Brongersma, Y. Cui, S. Fan, Light management for photovoltaics using high-index nanostructures, *Nat. Mater.* 13 (2014) 451.
[8] M.-W. Kim, K. Kim, T.Y. Ohm, H. Yoon, B. Joshi, E. Samuel, M.T. Swihart, S.K. Choi, H. Park, S.S. Yoon, Electrospayed BiVO₄ nanopillars coated with atomic-layer-deposited ZnO/TiO₂ as highly efficient photoanodes for solar water splitting, *Chem. Eng. J.* 333 (2018) 721–729.
[9] X. Xiao, R. Hu, C. Liu, C. Xing, C. Qian, X. Zuo, J. Nan, L. Wang, Facile large-scale synthesis of β-Bi₂O₃ nanospheres as a highly efficient photocatalyst for the degradation of acetaminophen under visible light irradiation, *Appl. Catal., B* 140 (2013) 433–443.
[10] V. Zhukov, V. Zhukovskii, V. Zainullina, N. Medvedeva, Electronic structure and chemical bonding in bismuth sesquioxide polymorphs, *J. Struct. Chem.* 40 (1999) 831–837.
[11] D. D'Angelo, S. Filice, A. Scarangella, D. Iannazzo, G. Compagnini, S. Scalese, Bi₂O₃/Nexar® polymer nanocomposite membranes for azo dyes removal by UV-vis or visible light irradiation, *Catal. Today* (2017), <https://doi.org/10.1016/j.cattod.2017.12.013>.
[12] L. Leontie, M. Caraman, M. Alexe, C. Harnagea, Structural and optical characteristics of bismuth oxide thin films, *Surf. Sci.* 507 (2002) 480–485.
[13] S. Kocuyigit, Boron and praseodymium doped bismuth oxide nanocomposites: preparation and sintering effects, *J. Alloys Compd.* 740 (2018) 941–948.
[14] F. Qin, G. Li, R. Wang, J. Wu, H. Sun, R. Chen, Template-free fabrication of Bi₂O₃ and (BiO)₂CO₃ nanotubes and their application in water treatment, *Chem. Eur. J.* 18 (2012) 16491–16497.
[15] Z.-C. Guan, H.-P. Wang, X. Wang, J. Hu, R.-G. Du, Fabrication of heterostructured β-Bi₂O₃-TiO₂ nanotube array composite film for photoelectrochemical cathodic protection applications, *Corrosion Sci.* 136 (2018) 60–69.
[16] Y. Sun, W. Wang, L. Zhang, Z. Zhang, Design and controllable synthesis of α-/γ-Bi₂O₃ homojunction with synergetic effect on photocatalytic activity, *Chem. Eng. J.* 211 (2012) 161–167.
[17] S. Dadashi, R. Poursalehi, Formation, gradual oxidation mechanism and tunable optical properties of Bi/Bi₂O₃ nanoparticles prepared by Nd: YAG laser ablation in liquid: dissolved oxygen as genesis of tractable oxidation, *Mater. Res. Bull.* 97 (2018) 421–427.
[18] Y. Qiu, M. Yang, H. Fan, Y. Zuo, Y. Shao, Y. Xu, X. Yang, S. Yang, Phase-transitions of α- and β-Bi₂O₃ nanowires, *Mater. Lett.* 65 (2011) 780–782.
[19] T. Thejaswini, D. Prabhakaran, M.A. Maheswari, Ultrasound assisted synthesis of nano-rod embedded petal designed α-Bi₂O₃-ZnO nanoparticles and their ultra-responsive visible light induced photocatalytic properties, *J. Photochem. Photobiol. A Chem.* 335 (2017) 217–229.
[20] M. Imran, A.B. Yousaf, M. Farooq, P. Kasak, Enhanced Z-scheme visible light photocatalytic hydrogen production over α-Bi₂O₃/CZS heterostructure, *Int. J. Hydrogen Energy* 43 (2018) 4256–4264.
[21] X. Liu, L. Pan, J. Li, K. Yu, Z. Sun, Visible light-induced photocatalytic activity of Bi₂O₃ prepared via microwave-assisted method, *J. Nanosci. Nanotechnol.* 13 (2013) 5044–5047.
[22] Y. Shen, Y. Li, W. Li, J. Zhang, Z. Hu, J. Chu, Growth of Bi₂O₃ ultrathin films by atomic layer deposition, *J. Phys. Chem. C* 116 (2012) 3449–3456.
[23] R. Chen, G. Cheng, M.H. So, J. Wu, Z. Lu, C.-M. Che, H. Sun, Bismuth subcarbonate nanoparticles fabricated by water-in-oil microemulsion-assisted hydrothermal process exhibit anti-Helicobacter pylori properties, *Mater. Res. Bull.* 45 (2010) 654–658.
[24] Q. Zhang, W. Gong, J. Wang, X. Ning, Z. Wang, X. Zhao, W. Ren, Z. Zhang, Size-dependent magnetic, photoabsorbing, and photocatalytic properties of single-crystalline Bi₂Fe₄O₉ semiconductor nanocrystals, *J. Phys. Chem. C* 115 (2011) 25241–25246.
[25] H. Yoon, M.G. Mali, J.Y. Choi, M.-W. Kim, S.K. Choi, H. Park, S.S. Al-Deyab, M.T. Swihart, A.L. Yarin, S.S. Yoon, Nanotextured pillars of electrospayed bismuth vanadate for efficient photoelectrochemical water splitting, *Langmuir* 31 (2015) 3727–3737.
[26] H. Yoon, M.G. Mali, M.-W. Kim, S.S. Al-Deyab, S.S. Yoon, Electrostatic spray deposition of transparent tungsten oxide thin-film photoanodes for solar water splitting, *Catal. Today* 260 (2016) 89–94, <https://doi.org/10.1016/j.cattod.2015.03.037>.
[27] M.-W. Kim, B. Joshi, H. Yoon, T.Y. Ohm, K. Kim, S.S. Al-Deyab, S.S. Yoon, Electrospayed copper hexaoxodivanadate (CuV₂O₆) and pyrovanadate (Cu₂V₂O₇) photoanodes for efficient solar water splitting, *J. Alloys Compd.* 708 (2017) 444–450.

- [28] M.-W. Kim, K. Kim, T.Y. Ohm, B. Joshi, E. Samuel, M.T. Swihart, H. Yoon, H. Park, S.S. Yoon, Mo-doped BiVO₄ nanotextured pillars as efficient photoanodes for solar water splitting, *J. Alloys Compd.* 726 (2017) 1138–1146.
- [29] B. Joshi, H. Yoon, H. Kim, M.-W. Kim, M.G. Mali, S.S. Al-Deyab, S.S. Yoon, Heterojunction photoanodes for solar water splitting using chemical-bath-deposited In₂O₃ micro-cubes and electro-sprayed Bi₂WO₆ textured nanopillars, *RSC Adv.* 5 (2015) 85323–85328.
- [30] P.M. Sirimanne, K. Takahashi, N. Sonoyama, T. Sakata, Photocurrent enhancement of wide bandgap Bi₂O₃ by Bi₂S₃ over layers, *Sol. Energy Mater. Sol. Cells* 73 (2002) 175–187.
- [31] C. Li, J. Zhang, K. Liu, A new method of enhancing photoelectrochemical characteristics of Bi/Bi₂O₃ electrode for hydrogen generation via water splitting, *Int. J. Electrochem. Sci.* 7 (2012) 5028–5034.
- [32] X. Lv, J. Zhao, X. Wang, X. Xu, L. Bai, B. Wang, Novel Bi₂O₃ nanoporous film fabricated by anodic oxidation and its photoelectrochemical performance, *J. Solid State Electrochem.* 17 (2013) 1215–1219.
- [33] X. Yang, X. Lian, S. Liu, G. Wang, C. Jiang, J. Tian, J. Chen, R. Wang, Enhanced photocatalytic performance: a β -Bi₂O₃ thin film by nanoporous surface, *J. Phys. D Appl. Phys.* 46 (2012), 035103.
- [34] K.C. Chitrada, R. Gakhar, D. Chidambaram, E. Aston, K.S. Raja, Enhanced performance of β -Bi₂O₃ by in-situ photo-conversion to Bi₂O₃-BiO_{2-x} composite photoanode for solar water splitting, *J. Electrochem. Soc.* 163 (2016) H546–H558.
- [35] K. Brezesinski, R. Ostermann, P. Hartmann, J. Perlich, T. Brezesinski, Exceptional photocatalytic activity of ordered mesoporous β -Bi₂O₃ thin films and electrospun nanofiber mats, *Chem. Mater.* 22 (2010) 3079–3085.
- [36] H. Cheng, B. Huang, J. Lu, Z. Wang, B. Xu, X. Qin, X. Zhang, Y. Dai, Synergistic effect of crystal and electronic structures on the visible-light-driven photocatalytic performances of Bi₂O₃ polymorphs, *Phys. Chem. Chem. Phys.* 12 (2010) 15468–15475.
- [37] D. Barreca, F. Morazzoni, G.A. Rizzi, R. Scotti, E. Tondello, Molecular oxygen interaction with Bi₂O₃: a spectroscopic and spectromagnetic investigation, *Phys. Chem. Chem. Phys.* 3 (2001) 1743–1749.
- [38] H. Fan, S. Pan, X. Teng, C. Ye, G. Li, L. Zhang, δ -Bi₂O₃ thin films prepared by reactive sputtering: fabrication and characterization, *Thin Solid Films* 513 (2006) 142–147.
- [39] S. Zhong, S. Zou, X. Peng, J. Ma, F. Zhang, Effects of calcination temperature on preparation and properties of europium-doped bismuth oxide as visible light catalyst, *J. Sol. gel Sci. Technol.* 74 (2015) 220–226.
- [40] H. Sudrajat, Chemical state and local structure of V species incorporated in δ -Bi₂O₃ photocatalysts, *J. Mater. Sci.* 53 (2018) 1088–1096.
- [41] Y. Shi, L. Luo, Y. Zhang, Y. Chen, S. Wang, L. Li, Y. Long, F. Jiang, Synthesis and characterization of α/β -Bi₂O₃ with enhanced photocatalytic activity for 17 α -ethynylestradiol, *Ceram. Int.* 43 (2017) 7627–7635.
- [42] L. Kumari, J.-H. Lin, Y.-R. Ma, One-dimensional Bi₂O₃ nanohooks: synthesis, characterization and optical properties, *J. Phys. Condens. Matter* 19 (2007), 406204.
- [43] A.L. Pereira, J.A. Sans, R. Vilaplana, O. Gomis, F. Manjón, P. Rodríguez-Hernández, A. Muñoz, C. Popescu, A. Beltrán, Isostructural second-order phase transition of β -Bi₂O₃ at high pressures: an experimental and theoretical study, *J. Phys. Chem. C* 118 (2014) 23189–23201.
- [44] K.C. Chitrada, K.S. Raja, R. Gakhar, D. Chidambaram, Enhanced photoelectrochemical performance of anodic nanoporous β -Bi₂O₃, *J. Electrochem. Soc.* 162 (2015) H380–H391.
- [45] C.-H. Ho, C.-H. Chan, Y.-S. Huang, L.-C. Tien, L.-C. Chao, The study of optical band edge property of bismuth oxide nanowires α -Bi₂O₃, *Optic Express* 21 (2013) 11965–11972.
- [46] L. Rekeb, L. Hamadou, A. Kadri, N. Benbrahim, Bi/ α -Bi₂O₃/TiO₂ nanotubes heterojunction with enhanced UV and visible light activity: role of Bismuth, *Electrochim. Acta* 256 (2017) 162–171.
- [47] B. Viswanathan, J.S. Lee, *Materials and Processes for Solar Fuel Production*, Springer, 2014.
- [48] F. Zaman, J. Kaewkhao, N. Srisittipokakun, N. Wantana, H. Kim, G. Rooh, Investigation of luminescence and laser transition of Dy³⁺ in Li₂O-Gd₂O₃-Bi₂O₃-B₂O₃ glasses, *Opt. Mater.* 55 (2016) 136–144.
- [49] G.W. Drake, *Springer handbook of Atomic, Molecular, and Optical Physics*, Springer Science & Business Media, 2006.
- [50] E.-J. Lee, S.-I. Pyun, Analysis of nonlinear Mott-Schottky plots obtained from anodically passivating amorphous and polycrystalline TiO₂ films, *J. Appl. Electrochem.* 22 (1992) 156–160.
- [51] M. Sharon, The photoelectrochemistry of semiconductor/electrolyte solar cells, *Encycl. Electrochem.* (2002) 287–316.
- [52] T.W. Kim, K.-S. Choi, Nanoporous BiVO₄ photoanodes with dual-layer oxygen evolution catalysts for solar water splitting, *Science* 343 (2014) 990–994.
- [53] K.J. McDonald, K.-S. Choi, A new electrochemical synthesis route for a BiOI electrode and its conversion to a highly efficient porous BiVO₄ photoanode for solar water oxidation, *Energy Environ. Sci.* 5 (2012) 8553–8557.
- [54] H. Weidong, Q. Wei, W. Xiaohong, D. Xianbo, C. Long, J. Zhaohua, The photocatalytic properties of bismuth oxide films prepared through the sol-gel method, *Thin Solid Films* 515 (2007) 5362–5365.
- [55] W. Xiaohong, Q. Wei, H. Weidong, Thin bismuth oxide films prepared through the sol-gel method as photocatalyst, *J. Mol. Catal. A Chem.* 261 (2007) 167–171.
- [56] A. Hameed, T. Montini, V. Gombac, P. Fornasiero, Surface phases and photocatalytic activity correlation of Bi₂O₃/Bi₂O_{4-x} nanocomposite, *J. Am. Chem. Soc.* 130 (2008) 9658–9659.
- [57] H.-Y. Jiang, J. Liu, K. Cheng, W. Sun, J. Lin, Enhanced visible light photocatalysis of Bi₂O₃ upon fluorination, *J. Phys. Chem. C* 117 (2013) 20029–20036.